Original Article

MOLECULAR METABOLISM

Hacd2 deficiency in mice leads to an early and lethal mitochondrial disease

Nahed Khadhraoui [1,2,3], Alexandre Prola [1,2,3], Aymeline Vandestienne [1,2,3], Jordan Blondelle [1,2,3], Laurent Guillaud [1,2,3], Guillaume Courtin [1,2,3], Maxime Bodak [1,2,3], Bastien Prost [4], Hélène Huet [5], Mélody Wintrebert [1,2,3], Christine Péchoux [6], Audrey Solgadi [4], Frédéric Relaix [1,2,3], Laurent Tiret [1,2,3,], Fanny Pilot-Storck [1,2,3,*]**

ABSTRACT

Objective: Mitochondria fuel most animal cells with ATP, ensuring proper energetic metabolism of organs. Early and extensive mitochondrial dysfunction often leads to severe disorders through multiorgan failure. *Hacd2* gene encodes an enzyme involved in very long chain fatty acid ($C \geq 18$) synthesis, yet its roles *in vivo* remain poorly understood. Since mitochondria function relies on specific properties of their membranes conferred by a particular phospholipid composition, we investigated if *Hacd2* gene participates to mitochondrial integrity.
Methods: We generated two mouse models, the first one leading to a partial knockdown of *Hacd2* expression and the second one, to a complete knockout of *Hacd2* expression. We performed an in-depth analysis of the associated phenotypes, from whole organism to molecular scale.
Results: Thanks to these models, we show that *Hacd2* displays an early and broad expression, and that its deficiency in mice is lethal. Specifically, partial knockdown of *Hacd2* expression leads to death within one to four weeks after birth, from a sudden growth arrest followed by cachexia and lethargy. The total knockout of *Hacd2* is even more severe, characterized by embryonic lethality around E9.5 following developmental arrest and pronounced cardiovascular malformations. In-depth mechanistic analysis revealed that *Hacd2* deficiency causes altered mitochondrial efficiency and ultrastructure, as well as accumulation of oxidized cardiolipin.
Conclusions: Altogether, these data indicate that the *Hacd2* gene is essential for energetic metabolism during embryonic and postnatal development, acting through the control of proper mitochondrial organization and function.

Keywords Phospholipid; Fatty acid; VLCFA; ELOVL; OXPHOS coupling; Heart development

1. INTRODUCTION

Mitochondria are double-membrane-bound organelles that provide most ATP energy through the oxidative phosphorylation (OXPHOS) process. OXPHOS relies on an electron transfer provided by the respiratory chain complexes nested in the inner membrane, which creates a proton gradient feeding the ATP synthase [1]. Impairment of OXPHOS leads to mitochondrial diseases, which is one of the most common and severe groups of inherited diseases [2—4]. Mutations in more than 250 genes of mitochondrial and nuclear genomes have been identified as the cause of mitochondrial diseases, yet molecular diagnosis is still lacking for many patients. Mitochondrial diseases are clinically diverse, affecting one or several organs and exhibiting prenatal to adult-onset. Because of their high energy demand, the brain, heart, muscle, liver, kidney, and endocrine organs are the most frequently affected organs in mitochondrial diseases, either alone or in any possible combination depending in part on the expression pattern and redundancy of the mutated gene [2,5,6]. Many genes associated with mitochondrial diseases are directly involved in OXPHOS, for example, encoding OXPHOS subunits or assembly factors. In parallel, many nuclear genes involved in mitochondrial diseases are indirectly required for OXPHOS, by ensuring proper mitochondrial organization. Among those are genes involved in mitochondrial membranes' morphology, dynamics, and membrane lipid composition.

A particular feature of mitochondria stands in the complex organization of its inner mitochondrial membrane (IMM), which folding into cristae relies on an exquisite interplay between proteins and lipids [7,8]. Notably, IMM organization requires cardiolipin (CL), an IMM-enriched four acyl-chain phospholipid. CL promotes a correct folding of the IMM, underlies the efficient organization of respiratory complexes, and allows the optimal function of the ATP synthase [9,10].

Cardiolipin and other membrane phospholipids often contain one or several acyl chains of 18 or more carbons, known as very long chain

[1]Univ Paris-Est Créteil, INSERM, IMRB, Team Relaix, F-94010 Créteil, France [2]EnvA, IMRB, F-94700 Maisons-Alfort, France [3]EFS, IMRB, F-94010 Créteil, France [4]UMS IPSIT, Université Paris-Saclay, Châtenay-Malabry, F-92296, France [5]Biopôle, École nationale vétérinaire d'Alfort, Maisons-Alfort, F-94700, France [6]Université Paris-Saclay, INRAE, AgroParisTech, GABI, F-78350, Jouy-en-Josas, France

*Corresponding author. Team Biology of the NeuroMuscular System, École nationale vétérinaire d'Alfort, 7 avenue du Général de Gaulle, 94700 Maisons-Alfort, France. E-mail: fanny.storck@vet-alfort.fr (F. Pilot-Storck).

**Corresponding author. Team Biology of the NeuroMuscular System, École nationale vétérinaire d'Alfort, 7 avenue du Général de Gaulle, 94700 Maisons-Alfort, France. E-mail: laurent.tiret@vet-alfort.fr (L. Tiret).

Received October 5, 2022 • Revision received January 13, 2023 • Accepted January 13, 2023 • Available online 21 January 2023

https://doi.org/10.1016/j.molmet.2023.101677

Abbreviations

AMP	adenosine monophosphate
AMPK	AMP kinase
ATP	adenosine triphosphate
BAT	brown adipose tissue
CL	cardiolipin
CS	citrate synthase
COX	cytochrome c oxidase
ELOVL	elongation of very long chain fatty acid protein
HACD	3-hydroxyacyl-CoA dehydratases
HREM	high-resolution episcopic microscopy
Hsd17b12	hydroxysteroid 17-beta dehydrogenase 12
IMM	inner mitochondrial membrane
KAR	3-ketoacyl-coA reductase
KD	knockdown
KO	knockout
OXPHOS	oxidative phosphorylation
TER	trans-2-enoyl-coA reductase
VLCFA	very long chain fatty acid
WT	wild type
WAT	white adipose tissue.

fatty acids (VLCFA) [8,11,12]. Contrarily to fatty acids < C18 synthesized in the cytosol by the Fatty Acid Synthase complex, VLCFA are elongated by an ER-embedded machinery through a four-step cycle [13]. The first step of condensation is catalyzed by fatty acids elongases encoded by seven different *ELOVL* genes [14]. The second and fourth steps of reduction are catalyzed by two unique enzymes, the 3-ketoacyl-coA reductase (KAR) and *trans*-2-enoyl-coA reductase (TER). The third step of dehydration is catalyzed by 3-hydroxyacyl-CoA dehydratases (HACD), encoded by four *HACD* genes [15,16]. While *ELOVL* genes have been largely investigated, characterization of *HACD* genes is still scarce despite evidence that *HACD1* mutations cause a congenital myopathy in humans, dogs and mice, characterized by a reduced muscle mass and strength [17–23]. More precisely, it was shown that *Hacd1* plays a crucial role in membrane phospholipid composition, both in muscle development and metabolism [19,22]. In particular, *Hacd1* deficiency impairs proper mitochondrial membrane composition and structure, which leads to a reduction in mitochondrial efficiency [22].

To date, no human mutation has been described for the *HACD2* gene, which product was shown in vitro to share a close structural and functional proximity with HACD1 [16]. A single northern blot performed on human tissues revealed a broad expression pattern of *HACD2* [24] and a recent article reported that a liver-specific knockout of *Hacd2* gene protected mice against diet-induced obesity [25]. To fill the lack of functional data on *Hacd2*, we generated a mouse line carrying a floxed allele at the *Hacd2* locus ($Hacd2^{flox}$), from which we derived knockout ($Hacd2^{KO}$) and conditional knockout ($Hacd2^{cKO}$) alleles to identify the roles of HACD2 during embryonic and postnatal development. We report here that knockout of *Hacd2* induces embryonic lethality at E9.5, and that knocking down *Hacd2* results in precocious death of mice in their first month of life. In both conditions, vital organs displayed reduced mitochondrial efficiency, representing a key feature of mitochondrial diseases. We further identified an alteration of mitochondrial ultrastructure and an accumulation of oxidized cardiolipins in *Hacd2* knockout embryos. Overall, our data show that *Hacd2* is an essential gene and a new member of mitochondrial disease-related nuclear genes.

2. RESULTS

2.1. Early and broad expression of the *Hacd2* gene

The $Hacd2^{flox}$ *and* $Hacd2^{KO}$ alleles contain a *LacZ* reporter gene in frame with exon 1 of the *Hacd2* gene (Fig. S1), driving expression of the β-galactosidase enzyme under the endogenous *Hacd2* promoter (Figs. S1A–B). We followed the expression pattern of *Hacd2* during development using X-Gal staining of whole-mount $Hacd2^{flox/+}$ and $Hacd2^{KO/+}$ embryos, which all displayed similar patterns regardless of the ES cell line (G09 or A10) they were derived from. At mid-embryonic development, we observed a ubiquitous expression in lineages derived from the three layers of the embryo, including the neural tube, heart, and somites (Figure 1A–C). Transverse sections of E9.5 embryo confirmed *Hacd2* expression in the endocardium and myocardium (Figure 1D–E).

In adult WT mice, RT-qPCR experiments confirmed a ubiquitous expression of the *Hacd2* gene, with a high expression in brown adipose tissue (BAT), white adipose tissue (WAT), kidney, liver, and testis; an intermediate expression in skin, brain, stomach, lung, and muscles; and a low, yet positive, expression in all other tested tissues (Figure 1F). This broad expression of the *Hacd2* gene was already present at day 9 after birth (P9), with the highest expression found in the liver and BAT (Figure 1G). In the adult heart, X-Gal staining revealed a strong expression in the nodal tissue, along with a low expression in the atria (Fig. S2).

2.2. *Hacd2* knockdown leads to a systemic disease resulting in cachexia

The strong splicing acceptor site at the 5' end of the *LacZ* construct was expected to favor splicing between the *LacZ* cassette and exon 1 of the *Hacd2* gene, at the expense of WT splicing of the *Hacd2* gene (Fig. S1). We thus expected that $Hacd2^{flox/flox}$ animals exhibit a knockdown of *Hacd2* expression. To assess the impact of a putative decrease of HACD2, we crossed $Hacd2^{flox/+}$ mice. Pups of the three expected genotypes were born, although at postnatal day 5 (P5), we counted a slightly reduced number of $Hacd2^{flox/flox}$ pups compared to the expected Mendelian ratio (analyzed pups n = 342, $Hacd2^{+/+}$ n = 100, $Hacd2^{flox/+}$ n = 180, $Hacd2^{flox/flox}$ n = 62). RT-qPCR experiments confirmed reduced levels of *Hacd2* mRNA in $Hacd2^{flox/flox}$ pups compared to their WT littermates, with the strongest reduction observed in the liver (- 88%), kidney (- 84%), BAT (- 85%) and heart (- 83%) (Figure 2A). The reduction was less pronounced in the skeletal muscle (- 54%). Overall, $Hacd2^{flox/flox}$ mice displayed a knockdown of *Hacd2* gene expression and will be hereafter named *Hacd2*-KD mice. When genotyped at P5, *Hacd2*-KD pups were indistinguishable from their WT and $Hacd2^{flox/+}$ littermates with the noticeable exception of a slightly reduced body mass (Figure 2B). From this stage on, and at a variable time point between P5 and P22, all observed *Hacd2*-KD pups experienced a growth arrest as visualized by their weight gain, and no survivor reached weaning age. More precisely, *Hacd2*-KD pups became more and more cachectic and lethargic within one to five days after their growth arrest, justifying their compassionate euthanasia (Figure 2C,D). At the terminal stage, growth retardation was illustrated by a lower body mass than their littermates (Fig. S3A), resulting from a reduced mass of several organs, including the liver, BAT and muscle (Fig. S3B). Morphological examination of the heart and large vessels, as well as a routine histological examination of the liver, kidney, and muscle did not identify abnormalities (Fig. S3C). Blood and marrow smear counts were within the normal range.

To identify the mechanisms responsible for this early, and rapidly fatal progression, we examined a panel of *Hacd2*-KD pups at P7, all asymptomatic and still growing. Blood analysis revealed hypoglycemia

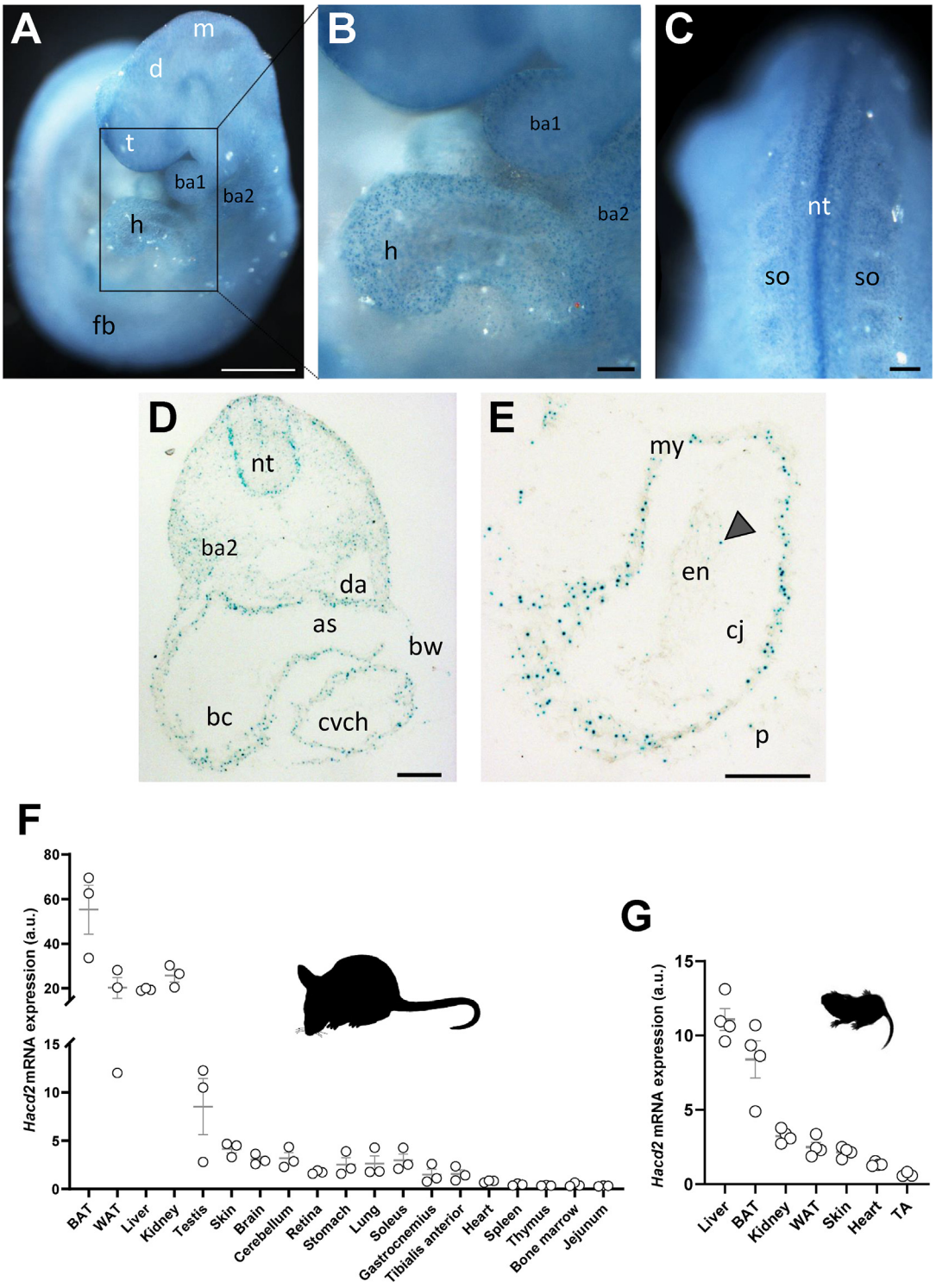

Figure 1: *Hacd2* expression during embryonic development and adulthood. **(A–E)** Expression pattern of *LacZ*-expressing cells on whole-mount **(A–C)** and transverse sections **(D,E)** of E9.5 *Hacd2*$^{KO/+}$ embryos. **(A)** At this stage, embryos have 20–22 pairs of somites, they have turned, and two pharyngeal bars and the forelimb are visible. After X-Gal staining, the embryo is uniformly blue, reflecting ubiquitous expression of *Hacd2*. **(B)** Focus on the region outlined in (A), showing *Hacd2* expression in the embryonic heart and branchial arches. **(C)** Dorsal view of the embryo showing *Hacd2* expression in the neural tube and somites. **(D)** All cell layers of the embryo express *Hacd2*, here on a transverse section at the level of the heart. **(E)** In the heart, staining is visible in the pericardium, myocardium and endocardium (arrowhead). **(F)** RT-qPCR quantification of *Hacd2* mRNA in adult WT mice, normalized to *Actin* mRNA. **(G)** RT-qPCR quantification of *Hacd2* mRNA in WT pups at postnatal day nine (P9), normalized to *Rpl32* mRNA. In (A–E), as is aortic sac; ba1, first branchial arch; ba2, second branchial arch; bc, *bulbus cordis*; bw, body wall, consisting in this region of pericardium and surface ectoderm; cj, cardiac jelly; cvch, common ventricular chamber of the heart; d, diencephalon; da, dorsal aorta; en, endocardium; fb, forelimb bud; h, heart; m, mesencephalon; my, myocardium; nt, neural tube; p, pericardium; so, somite and t, telencephalon. Scale bars are 500 μm in A and 100 μm in B-E. Individual data are plotted, along with the mean and standard error of the mean.

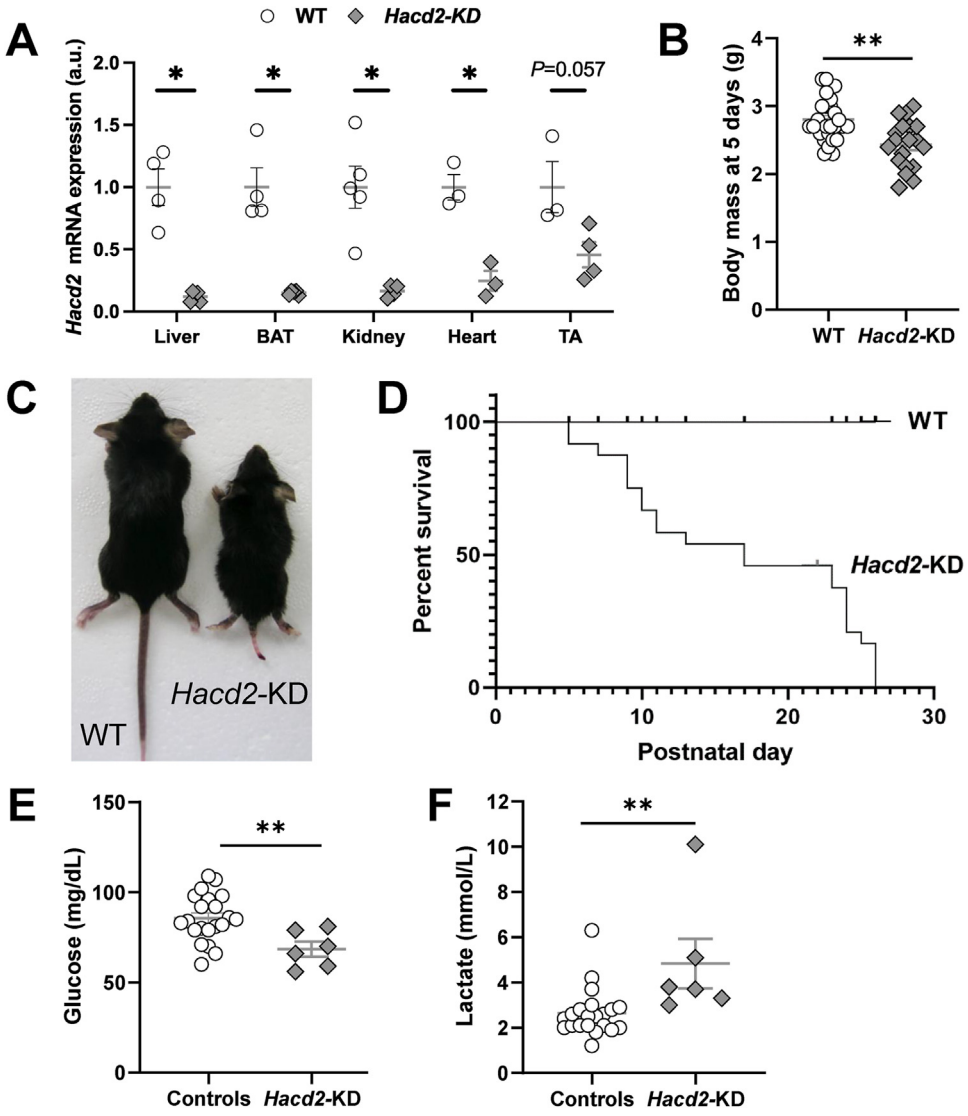

Figure 2: *Hacd2* knockdown leads to hyperlactatemia and lethality. **(A)** RT-qPCR quantification of *Hacd2* mRNA in tissues from WT and *Hacd2*-KD pups at P14, normalized to *Rpl32* mRNA. **(B)** Body mass of WT and *Hacd2*-KD pups at P5. **(C)** Representative picture of WT (left) and $Hacd2^{flox/flox}$ *(Hacd2-KD)* littermates at postnatal day 22 (P22). **(D)** Percent survival of *Hacd2*-KD pups compared to WT. **(E–F)** Glycemia **(E)** and lactatemia **(F)** in *Hacd2*-KD growing pups and control littermates at P7. Individual data are plotted, along with the mean and standard error of the mean. Individual data are plotted, along with the mean and standard error of the mean. *, $P < 0.05$; **, $P < 0.01$.

of these pups, accompanied by a 2-fold increase in lactatemia when compared to their littermates (Figure 2E,F).

The early excess of circulating lactate in the context of a devastating systemic disorder was evocative of a primary mitochondrial disease [2,3,6]. We thus evaluated respiratory capacities of the main vital organs of asymptomatic *Hacd2*-KD pups, while they were still growing. We quantified altered mitochondrial respiratory function in the kidney, liver and BAT, which remained unaffected in the heart and the *tibialis anterior* muscle (Table S1). We more precisely quantified phosphorylating and non-phosphorylating respiration rates, and the phosphorylating to non-phosphorylating ratio known as the respiratory control ratio. Both kidney and liver of *Hacd2*-KD pups were characterized by a marked decrease in the respiratory control ratio (−46% and −54%, respectively) (Table S1, Figure 3A–C, and E-G). These pups displayed a marked reduction of Cytochrome *c* oxidase (COX) activity staining on kidney cortex sections (Figure 3D). Following growth arrest, both citrate synthase (CS) and COX activity measured on kidney lysate tended to be reduced in *Hacd2*-KD pups (Fig. S4A), along with *Ppargc1a* gene expression (Fig. S4B), which suggested an absence of adaptative response in kidney.

Oppositely, COX activity tended to increase in liver lysate of *Hacd2*-KD pups (Fig. S4C), accompanied by a parallel increase in the expression of the *Cs* gene and genes involved in mitochondrial biogenesis such as *Ppargc1a, Nrf1,* and *Tfam* (Fig. S4D), which suggested an adaptative response of the liver to cope with a decreased mitochondrial coupling efficiency.

In the BAT, the respiratory control ratio was unchanged but phosphorylating and non-phosphorylating respiration were both significantly decreased (Figs. S4E–G). In accordance, BAT-related interscapular thermogenesis was reduced in *Hacd2*-KD pups (Fig. S4H), although their internal temperature was preserved (Fig. S4I), suggesting that the decreased coupling observed in other organs may serve as an alternative heat source for these pups.

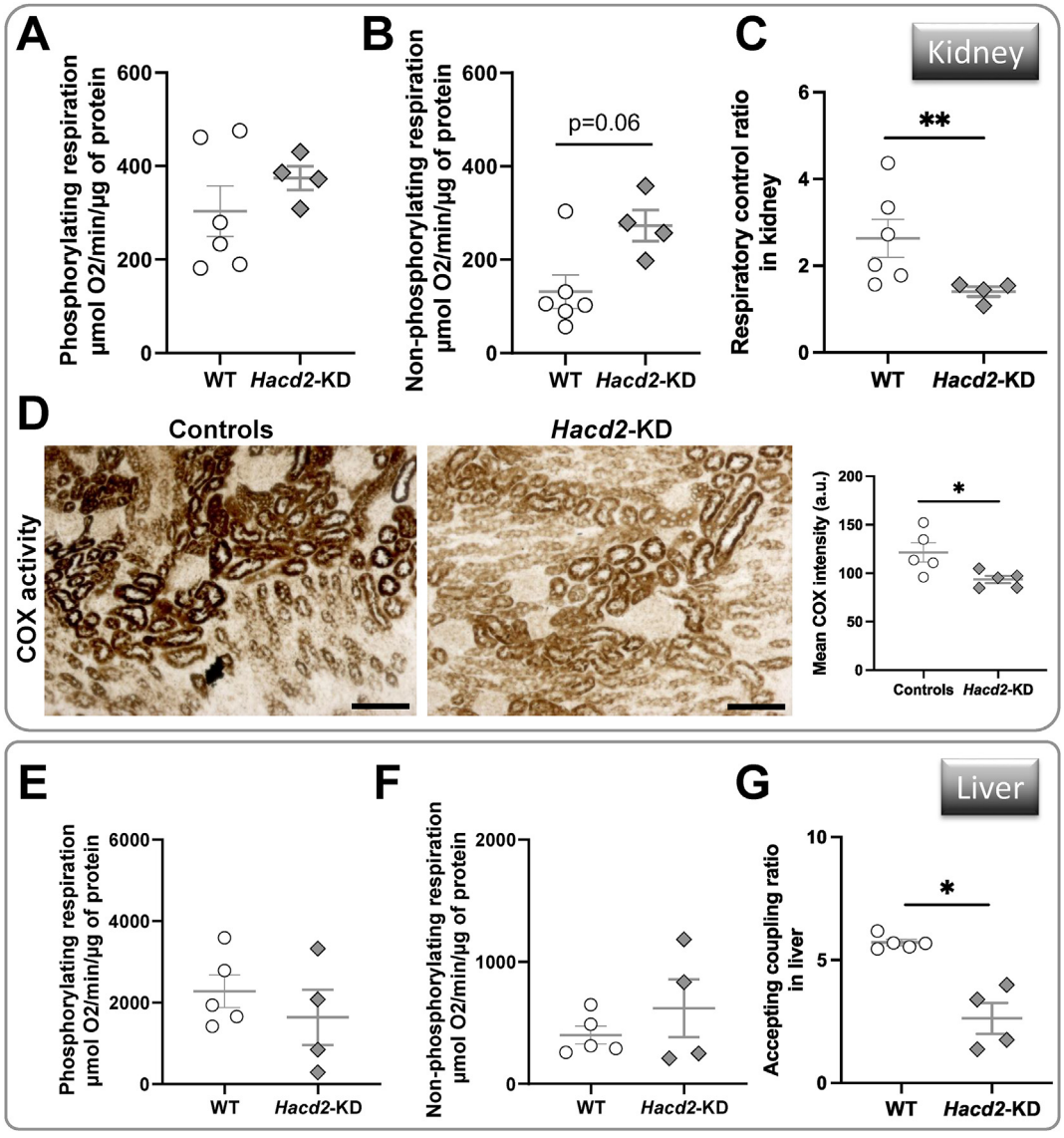

Figure 3: Impaired mitochondrial function in kidney and liver of *Hacd2*-KD mice. **(A–C)** Seahorse oxygraphy analysis on kidney homogenates. **(A)** Phosphorylating oxidation rate in the presence of pyruvate, malate, glutamate and succinate (Complex I and II). **(B)** Non-phosphorylating respiration after the addition of oligomycin. **(C)** Mitochondrial coupling (Respiratory Control Ratio, *i.e.* ratio of phosphorylating to non-phosphorylating oxidation rates from **A** and **B**). **(D)** COX activity staining and quantification in kidney cortex. **(E–G)** Seahorse oxygraphy analysis on liver homogenates. **(E)** Phosphorylating oxidation rate in the presence of pyruvate, malate, glutamate and succinate (Complex I and II). **(F)** Non-phosphorylating respiration after the addition of oligomycin. **(G)** Mitochondrial coupling (Respiratory Control Ratio, *i.e.* ratio of phosphorylating to non-phosphorylating oxidation rates from **E** and **F**). Data correspond to *Hacd2*-KD pups aged P9 to P14. Individual data are plotted, along with the mean and standard error of the mean. *, $P < 0.05$.

Lipidomic analysis of different organs of *Hacd2*-KD mice yielded no difference compared to WT for fatty acid and phospholipid content, as well as cardiolipin composition (Figs. S5 and S6).

Altogether, our data show that *Hacd2* knockdown induces a life-threatening systemic disease accompanied by early hyperlactatemia and impaired mitochondrial efficiency in the kidney and liver.

2.3. *Hacd2* knockout is embryonic lethal

To further examine the consequences of a full *Hacd2* deficiency, we crossed heterozygotes for the $Hacd2^{KO}$ allele. We never obtained mice of the $Hacd2^{KO/KO}$ genotype, whereas the two other genotypes followed the expected Mendelian ratios (48 analyzed pups, $Hacd2^{+/+}$ n = 16, $Hacd2^{+/KO}$ n = 32). This result suggested intra-uterine lethality. We thus interrupted the gestation of mice carrying *Hacd2*-KO embryos from progressively earlier stages. At embryonic day 11.5 post-coitum (E11.5) and then at E10.5, we observed very abnormal and delayed embryos with pericardial edema and an absence of salient cephalic vesicles, pigmented optic vesicles, protruding limb buds or well-defined branchial arches (Figure 4A). We noticed the first signs of embryonic resorption in some cases, evidenced by a truncated caudal part and a collapsed heart (Figure 4A).

We next analyzed $Hacd2^{KO/KO}$ (hereafter *Hacd2*-KO) embryos at E9.5. Genotyping revealed normal Mendelian ratios at this stage (285 analyzed embryos, $Hacd2^{+/+}$ n = 64, $Hacd2^{KO/+}$ n = 147, *Hacd2*-KO n = 74). WT and $Hacd2^{KO/+}$ littermates were indistinguishable, thus hereafter called control embryos. RT-qPCR analyses confirmed the complete lack of *Hacd2* mRNA expression in *Hacd2*-KO embryos (Fig. S7A), and in western blot a band at the expected size of HACD2 protein was present in WT embryos but absent in *Hacd2*-KO embryos

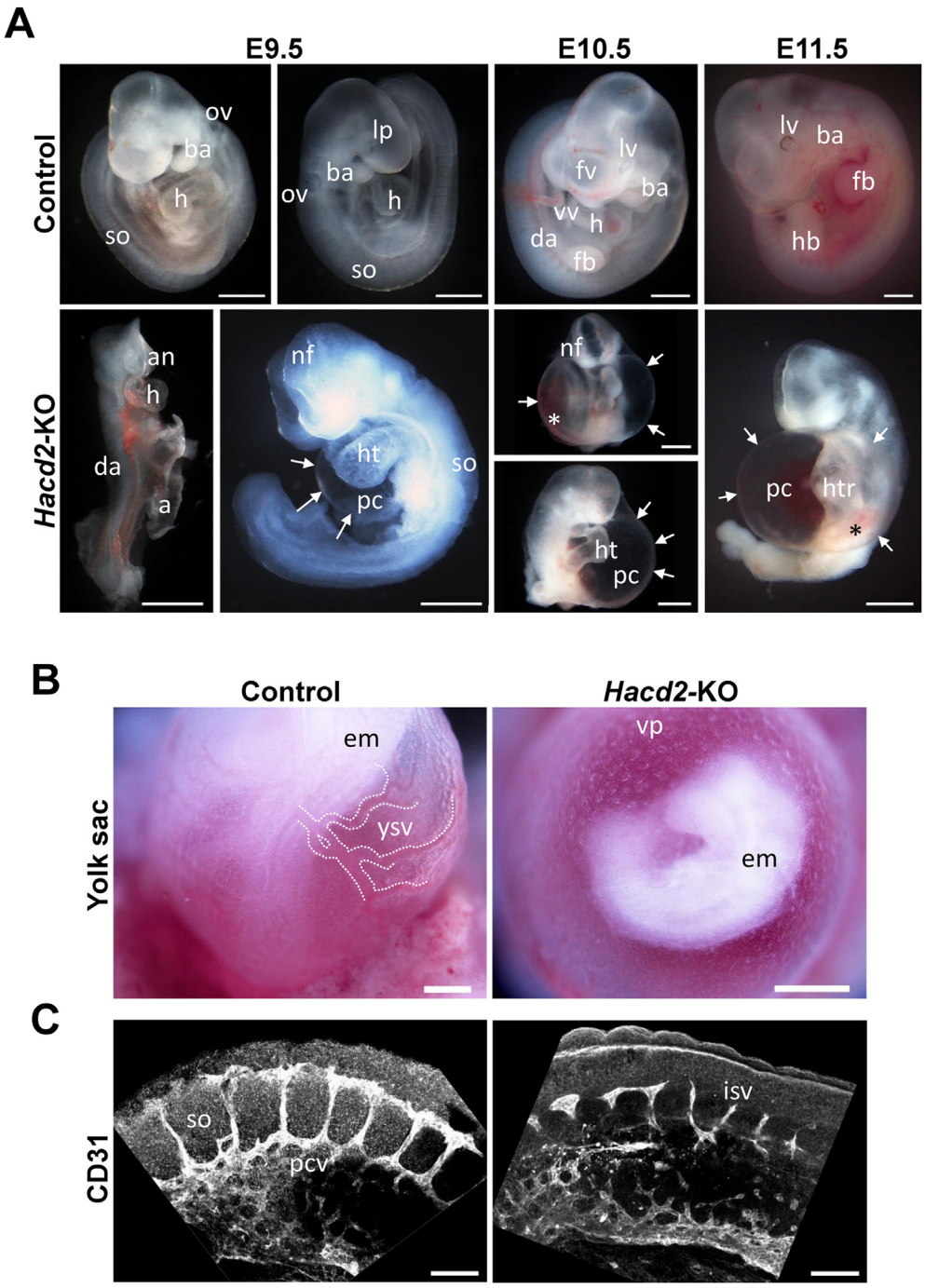

Figure 4: Anomalies of cardiovascular development in E9.5 *Hacd2*-KO embryos. **(A)** Representative control and knockout (*Hacd2*-KO) embryos from E9.5 to E11.5. Note the reduced size of *Hacd2-KO* embryos, some of them exhibit a poorly defined tail, rudimentary head parts with anterior and posterior neuropores still open. Most *Hacd2*-KO embryos display a pericardial edema (delimited by white arrows). Erythrocytes are visible in dorsal aorta, but they are seldom seen in head vessels and very often found sedimenting in the pericardial cavity (asterisk). In the most advanced embryos, the beating heart is not compartmentalized, in a U-shaped tubular form that contains no erythrocytes. **(B)** Representative pictures of the yolk sac surrounding the embryo. At this stage, yolk vascularization in the control is composed of vessels filled with red blood cells. These vessels form a tree-like network (part of which has been outlined by dotted lines) distributed over the entire surface of the sphere. In *Hacd2*-KO embryos, the early stage of a capillary plexus, formed of unconnected cell islands, is identifiable and no red blood cells are visible. **(C)** Z-stack in confocal microscopy of blood vessels revealed by labelling of endothelial cells with an anti-CD31 antibody. Vascular projections between somites are poorly visible in *Hacd2*-KO embryo, whereas they are regular and interconnected in the control. In (A), a is amnion; an, anterior neuropore; ba, branchial arch; da, dorsal aorta; fb, forelimb bud; fv, forebrain vesicle; h, heart; hb, hindlimb bud; ht, heart tube; htr, heart tube remnant; lp, lens placode; lv, lens vesicle; nf, neural folds; ov, otic vesicle; pc, pericardial cavity; so, somites and vv, vitelline vein. In (B), em is embryo; vp, vascular plexus and ysv, yolk sac vessel. In (C), isv is intersomitic vessel; pcv, posterior cardinal vein; so, somite. Scale bars are 500 μm in A and B and 100 μm in C.

(Fig. S7B), proving full efficiency of the genetic knockout strategy. At E9.5, all control embryos with 18–22 pairs of somites had turned and subdivision of the primitive brain vesicles was visible in the cephalic region, characterized by the closure of the anterior neuropore and a well-developed telencephalic vesicle. Two pairs of branchial arches, otic vesicles, and optic pits were visible (Figure 4A). On the contrary, all *Hacd2*-KO embryos had developmental delays evidenced by a smaller cephalic region with poorly defined subdivisions, and in many cases, the anterior neuropore remained open. Among these globally delayed embryos, we could distinguish two groups. In the first group (81% of the embryos), embryos had completed their turning, otic pits and branchial arches were visible (Figure 4A, right panel), but they exhibited fewer pairs of somites than expected, enabling to classify them as E9.0 to E9.25 embryos. Most of these embryos exhibited pericardial edema (Figure 4A), indicative of cardiovascular dysfunction. The second group (19%) was composed of embryos with even more pronounced stunted growth or developmental delay, evidenced by an incomplete turning. After removing annexes, they appeared as erected embryos that were staged as E8.5 embryos (Figure 4A, left panel).

2.4. *Hacd2* knockout leads to severe cardiovascular malformations

To further investigate the causes of this development arrest, we analyzed the *Hacd2*-KO embryos at E9.5, corresponding for most of them to the deviation stage from the normal course. Between E8.5 and E9.5, the total number of cells in the embryo and its annexes increases almost ninefold [26], and the establishment of a circulatory system accompanies this exponential growth. Indeed, beyond stage E7.5, the embryo's survival depends successively on the vascularization of the yolk sac and then on the proper embryonic circulation. We carefully checked the development of vascular networks and the heart and observed that the yolk sac of *Hacd2*-KO embryos was systematically devoid of the well-developed vessels observed in controls (Figure 4B). In *Hacd2*-KO embryos, vessel development was stopped at the honeycomb-shaped capillary plexus stage. No red blood cells were visible within these vascular anlagen.

Even in the most advanced E9.5 *Hacd2*-KO embryos, the heart never resembled a normally developed looped heart. In most cases, it remained at the heart tube stage (Figures 4A and S7C), a hallmark of the late E8.5 stage.

Analysis of histological sections or high-resolution episcopic microscopy (HREM) images allowed us to identify the presence of the three concentric pericardium, myocardium and endocardium cellular layers constituting the heart (Fig. S7C). However, the myocardium was always thinner than in controls. Because the primitive myocardium secretes cardiac jelly [27], we stained transverse sections with alcian blue that reveals hyaluronic acid of the cardiac jelly, and observed that it was produced in *Hacd2*-KO embryos, although in a lighter amount than in controls (Fig. S7D).

We then observed the internal vascularization of whole embryos. In both control and *Hacd2*-KO embryos, we confirmed the presence of a pair of dorsal aortae and umbilical veins, an anterior and a posterior cardinal vein, and a caudal vitelline vein, all lumenized (Fig. S7C). This indicated that vasculogenesis and angiogenesis proceeded appropriately. However, caudal expansion of the posterior cardinal vein and intersomitic vascular ramifications were poorly developed compared to controls (Figure 4C). Finally, although present in *Hacd2*-KO embryos (Figure 4A and S7C), red blood cells were accumulated in the venous network, rarely observed in dorsal aortae and in the cardiac chamber (Figures 4A and S7C).

In summary, *Hacd2* loss of function induced a vascularization defect of the yolk sac and the embryo, and an arrest of cardiac development at stage ~ E8.5. This arrest is concomitant with the looping morphogenetic movement that normally leads to the formation of a functional four-cavity heart [28]. In the heart, the myocardium was present. It secreted the cardiac jelly and contracted (Movie S1), revealing that myocardial cells had differentiated. However, these contractions were never accompanied by blood movement, likely because of the poor efficiency of the myocardium. Loss of function of the *Hacd2* gene thus causes an embryonic heart failure concomitant with a precocious termination of the embryo's development.

Supplementary video related to this article can be found at https://doi.org/10.1016/j.molmet.2023.101677

2.5. *Hacd2* expression in cardiovascular lineages is dispensable for embryonic development

We wondered whether the proper development of the embryonic cardiovascular system requires the cell-autonomous function of *Hacd2* in its constitutive lineages. To this end, we generated embryos lacking *Hacd2* early expression in the TEK (or TIE2)+ angioblast lineage yielding yolk sac and embryonic endothelial cells [29], or in the MESP1+ mesodermal cell lineage yielding precursor cells of the heart tube and the myocardium [30]. The selective inactivation of *Hacd2* in these lineages was obtained using the Cre recombinase expression under the *Tek* or the *Mesp1* gene promoter (Fig. S1C). In embryos expressing the $ROSA^{mTmG}$ allele [31], we validated that *Tek*-Cre was indeed expressed in the endothelium of vessels and the endocardium at E9.5, and that at this stage, *Mesp1*-Cre was broadly expressed in all lineages of the heart (Fig. S8A). We then crossed each of the two Cre lines with mice carrying the conditional *Hacd2*-cKO allele (Fig. S1C) and genotyped pups after birth. In both lines, we obtained mice invalidated for *Hacd2* in the targeted lineages in Mendelian proportion (five $Hacd2^{cKO/KO}$; *Tek*-Cre + individuals and six $Hacd2^{cKO/KO}$; *Mesp1*-Cre + individuals). They were all viable, showed no difference from their control littermates, and reached adulthood in healthy conditions. Accordingly, dissection of $Hacd2^{cKO/KO}$; *Tek*-Cre + embryos at E10.5 showed normal yolk sac vascularization and cardiovascular development (Fig. S8B). Likewise, echocardiographic parameters recorded in $Hacd2^{cKO/KO}$; *Mesp1*-Cre + adult mice were normal (data not shown). The efficiency of *Hacd2* inactivation in the heart of these mice was confirmed (Fig. S8C).

Consistently with the early ubiquitous embryonic expression of *Hacd2,* these results reveal that its essential role in cardiovascular development likely involves, at least in part, other lineages in a non-cell-autonomous process.

2.6. *Hacd2* knockout impairs mitochondrial energetic function

Given the mitochondrial dysfunction observed in the kidney and liver of *Hacd2*-KD pups and the observation that a severe impairment of OXPHOS or ATP synthase assembly also leads to lethality at mid embryonic development [32,33], we assessed mitochondrial function in *Hacd2*-KO embryos using a Seahorse device [33] (Table S2). Both phosphorylating and non-phosphorylating respirations were significantly reduced in *Hacd2*-KO embryos (Figure 5A–B), with a stronger impact on the phosphorylating respiration, leading to a marked reduction in the respiratory control ratio (Figure 5C). The respiratory chain's efficiency and the coupling between the respiratory chain and the ATP synthase were thus affected in *Hacd2*-KO embryos. This reduced mitochondrial efficiency was associated with a preserved mitochondrial mass, assessed by CS activity (Fig. S9A). Accordingly, we found no modification in the expression of the *Cs* gene and master coordinators of mitochondrial biogenesis (*Ppargc1a* and *Ppargc1b* genes and their target *Nrf1* gene) (Fig. S9B).

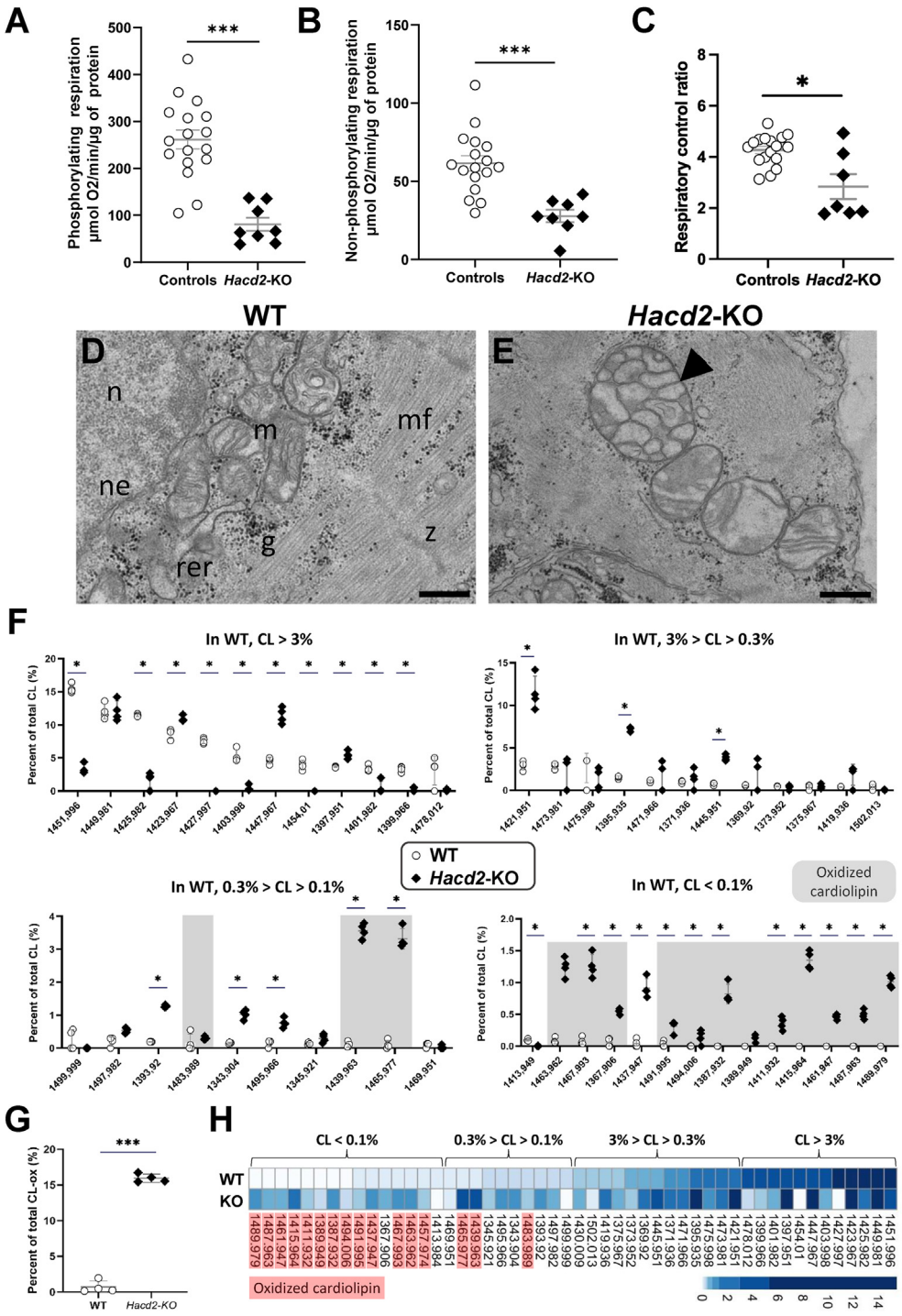

Figure 5: Impaired mitochondrial function in *Hacd2*-KO embryos. **(A–C)** Seahorse oxygraphy analysis of whole embryos homogenates at E9.5. **(A)** Phosphorylating oxidation rate in the presence of pyruvate, malate, glutamate and succinate (Complex I and II). **(B)** Non-phosphorylating respiration after the addition of oligomycin. **(C)** Mitochondrial coupling (Respiratory Control Ratio, *i.e.* ratio of phosphorylating to non-phosphorylating oxidation rates from **A** and **B**). **(D–E)** Transverse sections from E9.5 wild-type (WT) and *Hacd2*-KO embryos were examined by transmission electron microscopy. Images are representative of cells from the myocardium. **(D)** Ultrastructural organization of WT cells reveals an active rough endoplasmic reticulum and fields of mitochondria with evidence of tubular-shaped invaginations (cristae) of their internal membrane, unambiguously identified on the same plane than the outer membrane. Myocardial cells are identified by the presence of developing sarcomeres, organized between z-lines, adjacent to numerous glycogen rosettes. **(E)** Myocardial cells from age matched *Hacd2*-KO embryos display a rather normal global organization, with similar cytoplasm, nucleus and rough endoplasmic reticulum membrane systems. However, many mitochondria appear dilated and are abnormally compartmentalized (arrow heads). g, glycogen rosettes; m, mitochondrion; mf, myofibrils; n, nucleus; ne, nuclear envelope; rer, rough endoplasmic reticulum and z, z-line. Scale bars are 250 nm. **(F)** Repartition of cardiolipin species in WT and *Hacd2*-KO embryos according to their proportion in WT. Oxidized cardiolipin species are depicted on a grey background. **(G)** Relative percentage of oxidized cardiolipins in WT and *Hacd2*-KO embryos. **(H)** Heatmap of cardiolipin species in WT and *Hacd2*-KO embryos according to their repartition in WT. Oxidized cardiolipin species are highlighted in pink. Individual data are plotted, along with the mean and standard error of the mean. *, $P < 0.05$; ***, $P < 0.001$.

2.7. *Hacd2* knockout impairs mitochondrial membrane organization

Given the role of *Hacd2* in lipid synthesis and the alteration of the composition and structure of mitochondrial membranes in *Hacd1*-deficient muscles [22], we investigated the ultrastructural organization and the lipid composition of mitochondria in *Hacd2*-KO embryos.

First, using transmission electron microscopy, we carefully analyzed mitochondria ultrastructure in several tissues of different embryonic origins (*i.e.,* the myocardium, endocardium, pericardium, branchial arch, foregut, and ectoderm). In WT embryos, cristae density was variable even in the same cell, yet several cristae were visible in every mitochondrion and exhibited an elongated shape (Figure 5D and S9C–H). On the contrary, the vast majority of mitochondria in *Hacd2*-KO embryos showed abnormal cristae shape and organization, leading either to vesicle-like cristae or to the compartmentalization of mitochondria [34] (Figure 5E and S9C–H). This latter anomaly was salient in the myocardium, with 37% of mitochondria displaying compartmentalization in *Hacd2*-KO embryos, compared to 12% in WT embryos ($n = 3$ embryos per genotype, $P < 0.01$). Defective cristae structure associated with an alteration of respiratory parameters was suggestive of perturbations in cardiolipin metabolism, an IMM-specific phospholipid required for efficient OXPHOS process and proper cristae folding [9,10,22].

We analyzed total phospholipid content and the integrity of cardiolipin in *Hacd2*-KO embryos. We found an elevated phosphatidylserine relative content (Fig. S10A). On the contrary, cardiolipin relative content was unchanged (Fig. S10A), but an in-depth analysis of individual cardiolipin species revealed many oxidized cardiolipin species in *Hacd2*-KO embryos (Figures 5F and S10B, Table S3), yielding a total of 16% of oxidized cardiolipins in these embryos compared to 0.7% in WT (Figure 5G). This abundant presence of oxidized cardiolipin species provoked profound changes in cardiolipin species repartition when compared to WT embryos (Figure 5H). The expression of *Sod2, Gpx1* and *Catalase* genes that encode antioxidant enzymes was unchanged in *Hacd2*-KO embryos (Fig. S10C), which indicates that cardiolipin oxidation triggered no major antioxidative defense in this condition.

Altogether, these data suggest an early, broad, and essential role of *Hacd2* in IMM composition and organization that supports its requirement for efficient mitochondrial function in ATP production.

3. DISCUSSION

Our study revealed that *Hacd2* is an essential gene since the impairment of its expression is lethal, either in the first steps of organogenesis or in the first postnatal weeks, in knockout or knockdown conditions, respectively. Phenotypes associated with *Hacd2* deficiency are pleiomorphic: *Hacd2*-KO embryos exhibited major cardiac malformations, poor embryonic and extra-embryonic vascular development, and developmental delay, whereas *Hacd2*-KD pups failed to thrive and evolved to fatal cachexia and lethargy. Such devastating syndromic conditions are evocative of mitochondrial diseases. The hypothesis of a role played by HACD proteins in mitochondrial function was recently confirmed for HACD1 in muscle [22]. Here, we demonstrated severe mitochondrial dysfunction in *Hacd2*-KO embryos and the kidney and liver of *Hacd2*-KD pups. These phenotypes are reminiscent of the most severe forms of mitochondrial diseases in human patients, which are associated with abortion or lethality in early postnatal life despite intensive care [2,3,6].

In patients, early and devastating mitochondrial disorders often involve several organs, yet their precise involvement is generally poorly resolved [3,6]. Here, we have demonstrated a reduced mitochondrial coupling in the kidney and liver of *Hacd2*-KD pups from early stages. Hyperlactatemia and hypoglycemia are critical biological anomalies associated with severe mitochondrial diseases [3,6] and were both present in *Hacd2*-KD pups from early stages. This pointed to a primary mitochondrial disease and indicated lactic acidosis as the likely cause of the fatal deterioration observed in *Hacd2*-KD pups. At this stage, we neither have identified any alteration in the fatty acid or phospholipid content nor in the cardiolipin composition of the affected organs. Further investigations will be necessary to elucidate the subtle and probably combined lipid abnormalities associated with the *Hacd2*-KD phenotype.

Hacd2-KO embryos were characterized by a developmental delay and an abnormal cardiovascular development that were lethal around E9.5. Cardiac malformation was associated with the absence of blood flow and pericardial oedema despite cardiac beating, suggesting insufficient contractile force of the myocardium. Vascular development was also failing, with thin and short peripheral vessels, and an absence of visible vessels in the yolk sac. Global embryonic development was altered, with embryos often presenting reduced growth, incomplete turning, reduced tail part and delayed head development. This systemic phenotype could result from heart dysfunction and the subsequent absence of blood flow led us to test the hypothesis of a cardiac-autonomous requirement for *Hacd2* expression. Conditional knockout of *Hacd2* in cardiac and endothelial cell lineages did not reproduce the *Hacd2*-KO phenotype, rather suggesting that *Hacd2* role in cardiovascular development can be compensated by other *Hacd2*-expressing structures, perhaps through the diffusion of products synthesized by the VLCFA elongation pathway.

We demonstrated mitochondrial dysfunction in whole embryo homogenates, associated with abnormal mitochondrial ultrastructure observed in all the analysed lineages, which reflects a broad requirement of *Hacd2* expression for mitochondrial organization and function. Thus, although cardiovascular malformations are likely the leading cause of embryonic lethality, *Hacd2*-KO embryos presumably suffered from a systemic mitochondrial defect.

Our study thus confirms the role of the VLCFA elongation cycle in mitochondrial homeostasis [22,35]. More precisely, mitochondrial dysfunction in *Hacd2*-KO embryos, and in the kidney and liver of *Hacd2*-KD pups, affected both the respiratory chain complexes and respiratory coupling. This mitochondrial defect is more pronounced than in *Hacd1*-deficient muscle fibres in which respiratory coupling was markedly reduced with spared respiratory complexes [22]. In *Hacd1*-deficient muscle fibres, cardiolipin depletion was responsible for the reduction of mitochondrial coupling, linking HACD1 enzymatic activity to mitochondrial phospholipids synthesis [22]. Notably, this reduced mitochondrial coupling leads to a higher energy expenditure in *Hacd1*-KO mice and protects them against diet-induced obesity. This metabolic shift is also shared by liver-specific *Hacd2*-KO mice [25], which is consistent with the evidence demonstrated here of a control of mitochondrial efficiency in the liver by *Hacd2*.

Severe alteration of cardiolipin biosynthesis has been associated with defective respiratory complex assembly and function, and early embryonic lethality in mice [36–39]. Here, *Hacd2*-KO embryos displayed high amounts of oxidized cardiolipin that likely contribute to mitochondrial dysfunction. Indeed, cardiolipin is highly sensitive to oxidation because of its high content in polyunsaturated fatty acids and oxidized cardiolipins undergo conformational changes that impair OXPHOS activity and induce the release of apoptotic factors, ultimately triggering cell death [40–42].

Our study thus highlights the essential role of the VLCFA elongation cycle in embryonic development through mitochondrial homeostasis.

Previous data identified that knocking out *Hsd17b12*, which encodes KAR protein, leads to severe developmental defects and embryonic arrest at E9.5 [43]. Here, we reveal that knocking out *Hacd2* induces a close phenotype, and we propose a molecular and cellular explanation targeting a mitochondrial dysfunction.

4. CONCLUSION

We identified that *Hacd2* deficiency is responsible for severe and early mitochondrial disease and demonstrated an early requirement of *Hacd2* for mitochondrial organization and function. This suggests including *Hacd2* in the list of genes targeted for mitochondrial disease diagnosis, with priority given to the search for hypomorphic variants.

5. MATERIALS AND METHODS

- EXPERIMENTAL MODEL AND SUBJECT DETAILS
- DETAILED METHODS
  - o Generation of *Hacd2*-deficient mice
  - o Extraction and PCR analysis of genomic DNA
  - o Extraction of total RNA, RT-PCR and RT-qPCR analyses
  - o Western blot experiments
  - o Tissue and embryo collection
  - o X-Gal staining of embryos
  - o Histological staining
  - o Acetylcholinesterase activity
  - o Immunofluorescence
  - o High-Resolution Episcopic Microscopy (HREM) imaging
  - o Transmission electron microscopy
  - o Enzymatic assays
  - o Respiration measurement
  - o Lipidomic analyses
  - o Determination of glucose and lactate blood concentration
  - o Temperature measurement
- QUANTIFICATION AND STATISTICAL ANALYSES

6. EXPERIMENTAL MODEL AND SUBJECT DETAILS

Experiments on mice were approved by the Anses/EnvA/Upec Ethics Committee (C2EA — 16; approval number 20/12/12—17 and 17—031) and all care and manipulations were performed in accordance with national and European legislation on animal experimentation (EU Directive 2010/63/EU for animal experiments). The whole study was carried on animals that were housed in stainless steel cages containing environmental enrichment, in rooms maintained at 22 ± 1 °C with an air change rate of 12 vol/h and lit from 7am to 7pm. Food and water were given *ad libitum*. Food was breeding diet for rats and mice (C1314, Altromin) for pregnant and lactating females or maintenance diet (C1324, Altromin) for weaned animals. All animals received neutral pH water.

7. DETAILED METHODS

7.1. Generation of *Hacd2*-deficient mice

Three clones of recombinant ES cells with a tm1a(EUCOMM)Hmgu allele at the *Hacd2* locus (MGI:1918007; clones A10, E11 and G09) were obtained from the EUCOMM consortium (www.mousephenotype.org) and were injected into host blastocysts. Southern blot of genomic DNA confirmed for all three clones a unique insertion of the recombination vector at the *Hacd2* locus. Chimeras derived from the E11 clone did not transmit the recombinant allele. Independent *Hacd2* mutant lines were established from the two A10 and G09 clones.

Mice carrying the *Hacd2* targeting allele ($Hacd2^{flox}$, further named $Hacd2^{KD}$) were bred with *PGK-Cre* mice to generate *Cre*-positive mice carrying a recombinant, knockout *Hacd2* ($Hacd2^{KO}$) allele lacking exon 2 and the *NeoR* cassette (Fig. S1). In parallel, mice carrying the $Hacd2^{flox}$ allele were bred with *act-Flp* mice to generate *Flp*-positive mice carrying a recombinant allele lacking *LacZ* and *NeoR* cassettes, suitable for conditional knockout ($Hacd2^{cKO}$ allele; Fig. S1). Eventually, we generated an *Hacd2* allele lacking exon 2 and the *LacZ* and *NeoR* cassettes ($Hacd2^{completeKO}$) by sequentially crossing $Hacd2^{flox}$-bearing mice with *act-Flp*-bearing mice and then with *PGK-Cre*-bearing mice. In all cases, *PGK-Cre* and *act-Flp* transgenes were eliminated at the following generation. We confirmed the complete similarity of $Hacd2^{KO/KO}$ and $Hacd2^{completeKO/completeKO}$ embryos and further performed the experiments on $Hacd2^{KO/+}$ crosses. All experiments were performed on mice generated from the two independent ES clones. Littermates from crosses between $Hacd2^{+/flox}$ males and females were identified and genotyped at postnatal day 5 and weighted every day. When no weight gain was observed for $Hacd2^{flox/flox}$ pups compared to the day before, this corresponded to their growth arrest and they were euthanized within 2 days.

To generate *Hacd2* conditional knockout, we first crossed *Mesp1-Cre*- or *Tek-Cre*-bearing mice with *mTmG*-bearing mice to check the conversion of RFP to GFP signal in *Mesp1*-or *Tek*-expressing tissues, respectively. We then crossed $Hacd2^{cKO/+}$ mice with *Mesp1-Cre*- or *Tek-Cre*-bearing mice and mice bearing both alleles were further crossed with $Hacd2^{KO/+}$ mice to obtain $Hacd2^{cKO/KO}$; *Mesp1*-or *Tek-Cre* + mice and control littermates.

7.2. Extraction and PCR analysis of genomic DNA

Mouse embryos were harvested at specific developmental stages from timed pregnant females. Embryos were dissected under a stereomicroscope (Nikon SMZ1500).

For pups from $Hacd2^{KD/+}$ crosses, we sectioned a finger at P5 for genotyping and identification. For embryos, we carefully removed the yolk sac, avoiding contamination with maternal tissues. Genotyping was performed on yolk sac and finger lysates. Samples were incubated 20 min at 99 °C in 50 µl or 200 µL (yolk sac and finger, respectively), of a 25 mM NaOH, 0.2 Mm EDTA buffer, then the same volume of a 40 mM Tris buffer pH5 was added, followed by centrifugation 2 min at 20,000 rcf.

Primers used for genotyping for *Hacd2* alleles are shown in the Table S4. Primers used to detect the *PGK-Cre*, *Mesp1-Cre*, *Tek-Cre* or *act-FLP* transgene are shown in Table S5.

7.3. Extraction of total RNA, RT-PCR and RT-qPCR analyses

Samples were snap-frozen in liquid nitrogen and stored at −80 °C. Total RNAs were isolated using either TRIzol reagent (Sigma) for tissues or RNeasy plus micro kit (Qiagen) for embryos according to the manufacturer's protocol. Purity of RNAs was assessed by a ratio of absorbance at 260 nm and 230 nm > 1.8. RNA quality was checked on agarose gel. 200 ng of RNA were used for reverse transcription with the Maxima First Strand cDNA Synthesis Kit for RT-qPCR (Fermentas). cDNA was amplified using the Maxima SYBR Green qPCR Master Mix (2X; Fermentas). qPCR reactions were performed on a Roche Light Cycler system (Roche). qPCR products were examined qualitatively on agarose gels. All the primers used are listed in Table S5.

7.4. Western blot experiments

Frozen tissues were lysed in RIPA lysis buffer (50 mM Tris—HCl, pH 8, 150 mM NaCl, 1% Triton, 1 mM EDTA, 0.1% SDS, 0.5% deoxycholic acid), supplemented with a cocktail of protease and phosphatase inhibitors (Pierce), using a Precellys homogenizer (Bertin). Protein concentration was assessed using the bicinchoninic acid assay (Pierce BCA Protein Assay Kit −23225). Protein extracts from embryos were loaded on Bolt™ 4—12% Bis-Tris gels (Invitrogen), separated for 22 min at 200 V and subsequently transferred to PVDF membranes using transfer stack and iblot2 system for 7 min at 20 V (Invitrogen). Thereafter, blots were blocked for 1 h in 5% BSA and 0.1% Tween20 in TBS pH 7.4 (20 mM Tris, 150 mM NaCl) at room temperature, followed by incubation with the primary antibody anti-HACD2 (orb33286 from Biorbyt; 1:1000) overnight at 4 °C. After washing, membranes were incubated with an HRP-conjugated anti-rabbit antibody for 1 h at room temperature and revealed using the West Femto chemiluminescent substrate (Pierce). Light emission was recorded using a chemiluminescent detection system (G-Box, Syngene) and quantified by ImageJ software (v1.47, NIH).

7.5. Tissue and embryo collection

Mice were killed by cervical dislocation for animals older than three weeks, or by section of the head for mice up to three weeks, in accordance with the principles of good laboratory animal practice.

After removal, the organs were rinsed with phosphate buffered saline (PBS). Direct freezing in liquid nitrogen was carried out for RNA extraction. Freezing in liquid nitrogen-cooled liquid isopentane was carried out for cryostat sectioning. For X-Gal staining or histological analyses, organs were fixed in formol (4% formaldehyde in PBS) during 30 min or several days, respectively.

According to the vaginal plug, pregnant females carrying embryos expected to be between E9.5 and E11.5 were killed by cervical dislocation. Their pregnant uterine horns were exposed by laparotomy. When visualization of vitelline and embryonic blood vessels was required, the female and its uterine horns, left attached, were placed on ice for 30 min, which allowed for the retention of red blood cells in the so-colored vessels. For other experiments, uterine horns were removed immediately. All uterine horns were placed in a Petri dish containing PBS prechilled on ice. Incision was made along the large curvature of each uterine horn, and the fetal envelopes were removed using thin forceps to access directly to the embryo surrounded by its amniotic sac. The embryos were then rinsed in PBS and directly observed or processed as required for the different experiments. All observations of the embryos were done using a Nikon SMZ1500 stereo microscope and images were acquired using NIS software (Nikon). Precise staging was assessed by counting pairs of somites and by observing morphological features specific of each Theiler's stage and confirmed the expected stage of embryos.

7.6. X-Gal staining of embryos

For X-Gal staining, the embryos were fixed in 1% formaldehyde in PBS for 15 min (embryos at E9.5) or 20 min (embryos at E10.5 or E11.5), then rinsed in PBS and immersed overnight at 33 °C in the absence of light, in a solution of X-Gal (4 mM potassium ferrocyanide, 4 mM potassium ferricyanide, 2 mM $MgCl_2$, 1% *sodium deoxycholate*, 1% Nonidet P40, 4% 5-Bromo-4-chloro-3-india-BD-Galactopyranoside or X-Gal, in PBS). The next day, the embryos were rinsed in PBS and observed.

After freezing in OCT embedding medium (Tissue-Tek) in isopentane precooled in liquid nitrogen and storage at −80 °C, E9.5 embryos and adult heart from *Hacd2*$^{+/KO}$ mice were cut with a cryostat with a thickness of 10 μm for embryos and 20 μm for heart and sections were deposited on Superfrost slides. After taking out of the freezer at −80 °C, the slides were dried and fixed as previously described and then immersed overnight at 33 °C in the absence of light, in a solution of X-Gal. The next day, slides were rinsed in PBS and mounted using aqueous mounting medium (Dako Faramount).

7.7. Histological staining

Kidneys and livers were fixed in buffered formalin solution 10% (v/v) for 24 h. They were then clarified, dehydrated in successive baths of ethanol (70%—100%) and finally included in paraffin according with the routine process automatically with LOGOS ONE (Microm Microtech France, Brignais, France). They were embedded into blocks of paraffin. Embryos were fixed in in buffered formalin solution 10% (v/v) for 20 min and embedded of agarose 1.3% for subsequent manipulations. They were similarly processed for inclusion, individually oriented and embedded into blocks of paraffin. Tissue sections (3.5 μm) were cut with Leica RM 2245 (Leica Microsystems, Wetzlar, Germany).

Tibialis anterior muscles were processed through cryostat sectioning. Sections were then stained with hematoxylin and eosin or acidic alcian blue.

For COX activity, kidneys were frozen in OCT embedding medium (Tissue-Tek) in isopentane precooled in liquid nitrogen, and then stored at −80 °C. Tissue sections (10 μm) were fixed for 30 min in formol and stained for COX activity in a 20 mM KH_2PO_4, 80 mM Na_2HPO_4, 30 μM 3,3′-diaminobenzidine, 1 μM Cytochrome C buffer.

Images were captured using an Axio Observer Z1 microscope (Zeiss) and analyzed in a blinded manner using the ImageJ software (v1.47, NIH).

7.8. Acetylcholinesterase activity

Heart sections from *Hacd2*$^{+/KO}$ mice were prepared as for X-Gal staining. Histochemical localization of acetylcholine esterase (AchE) activity in the conduction system was performed with the esterase reaction (Karnowsky and Roots reaction). Briefly, we prepared a solution containing 0.173 mM acetylthiocholine iodide, 0.01 mM *tetraisopropyl pyrophosphoramide* (iso-MPA), 60 mM sodium acetate, 5 mM sodium citrate, 3 mM cupric sulfate and 5 mM of potassium ferricyanide in PBS. Three hundred microliters of this solution were put on sections for 30 min and then rinsed with PBS.

7.9. Immunofluorescence

Embryos were fixed in 1% formaldehyde in PBS for 1 h, rinsed twice in PBS for 30 min and then blocked and permeabilized with 3% BSA and 0.1% Triton X-100 in PBS for 7 h at 4 °C, followed by incubation with primary antibody at 4 °C overnight. We used the CD31 antibody (PECAM1; BD, 553370; 1:500 dilution). Embryos were then rinsed three times with 3% BSA and 0.1% Tween in PBS and incubated for 1 h at room temperature with a fluorophore conjugated anti-rat antibody Alexa-fluor555 (A-21434) and Alexa-fluor647 (A-21247), respectively (Thermofisher; 1:500 dilution). Embryos were finally rinsed twice in PBS for 30 min. Images were acquired on a confocal microscope (Zeiss LSM 800).

7.10. HREM imaging

High Resolution Episcopic Microscopy was performed on E9.5 embryos as described [44], using the optical high-resolution microscope (indigo Scientific). Resulting datasets comprised 700—1200 images of 1 * 1 μm size produced by repeated removal of 1—2 μm sections.

7.11. Transmission electron microscopy

Samples were processed for transmission electron microscopy at the MIMA2 platform (https://doi.org/10.15454/1.5572348210007727E12).

Tibialis anterior muscle, kidney, a small piece of liver, and the apical part of heart, or embryos, were fixed with 2% glutaraldehyde in 0.1 M sodium cacodylate buffer, pH 7.2, at 4 °C overnight. Samples were contrasted with Oolong Tea Extract 0.5% in cacodylate buffer; post-fixed with a solution of 1% osmium tetroxide and 1.5% potassium cyanoferrate; gradually dehydrated in ethanol (30%—100%) and substituted gradually in a mix of propylene oxyde-epon and embedded in Epon (Delta microscopy). Thin sections (70 nm) were collected onto 200 mesh copper grids, and counterstained with lead citrate. Grids were examined with a Hitachi HT7700 electron microscope operating at 80 kV (Milexia). Images were acquired with a charge-coupled device camera (AMT).

7.12. Enzymatic assays

Small pieces of frozen tissues or embryos were homogenized in an ice-cold buffer (one ml for 20 mg of tissue or a pool of two embryos) containing 5 mM Hepes, pH 8.7, 1 mM EGTA, 1 mM DTT and 0.1% Triton X-100, using a Precellys homogenizer (Bertin), by 2 cycles of 8 s at 6,500 rpm. Protein concentration was assessed using the bicinchoninic acid assay (Pierce BCA Protein Assay Kit −23225). Total activity of cytochrome oxidase (COX) and citrate synthase (CS) was assayed at 30 °C, pH 7.5, using standard spectrophotometric assays [45].

7.13. Respiration measurement

Single fresh mouse embryos or weighted pieces of tissues were homogenized in the assay medium (70 mM sucrose, 220 mM mannitol, 10 mM KH_2PO_4, 5 mM $MgCl_2$, 2 mM HEPES, 1 mM EGTA, 0.2% BSA; pH 7.2) containing substrates for Complex I (10 mM pyruvate, 2 mM malate, 10 mM glutamate) and 2 mM ADP. Homogenization was performed in a Dounce homogenizer (Sigma) in 500 µl of buffer for embryos or 1 ml for tissues. One hundred up and down strokes with Dounce pestle A were performed at 4 °C. The homogenate was then passed through a 100 µm cell strainer into a 50 ml polypropylene Falcon tube. Homogenates (the whole homogenates for embryos, or a quantity equivalent to 125 µg for liver, 150 µg for kidney and heart, 7.5 mg for TA and 50 µg for BAT, based on the weighting of fresh tissues) were transferred to XF-V7 24-well plates (Seahorse Bioscience) and spun down for 20 min at 2000 g, 4 °C (final volume 500 µl per well). The oxygen consumption rate was determined at 37 °C according to manufacturer's acquisition parameters used for Seahorse Cell Mito Stress Test. Respiration was determined with complex I substrates and ADP (Complex I) and then after subsequent addition of 10 mM succinate (Complex I + II or phosphorylating respiration), 2 µM oligomycin (non-phosphorylating respiration) and 0.4 µM antimycin A (non-mitochondrial respiration). Respiration rates were derived by subtracting non-mitochondrial respiration following addition of antimycin A. The respiratory control ratio (RCR) was determined by calculating the ratio of phosphorylating respiration on non-phosphorylating respiration. At the end of the run, cells from the wells were collected by up and down pipetting, transferred into tubes, and centrifuged to discard the supernatant. Two successive washes of the pellet were done with PBS, then protein quantification was performed using the bicinchoninic acid assay (Pierce BCA Protein Assay Kit −23225).

7.14. Lipidomic analyses

Tissues from WT and *Hacd2*-KD mice were collected immediately after euthanasia. For fatty acid and phospholipid analysis, tissues from P8 to P13 mice were frozen in liquid nitrogen and protected from oxidation by a layer of argon gas and stored at −80 °C until analysis. These analyses were performed as described in [19]. For mitochondrial phospholipid analyses, mitochondria were isolated from P18 to 25 mice. For the isolation of mitochondria from the heart, hearts were quickly collected in ice-cold DPBS (Gibco), minced and homogenized with a Dounce (100 up and down strokes with pestle A) in 5 ml of ice-cold mitochondria isolation buffer (MIB; 310 mM sucrose, 20 mM Tris—HCl, 1 mM EGTA, pH 7.2). Mitochondria were purified by differential centrifugation (1200*g* for 10 min) and supernatants were then centrifuged at 12000*g* for 10 min. For the isolation of mitochondria from the liver and kidney, the same protocol was applied with a different mitochondrial isolation buffer (MIB2; 200 mM sucrose, 10 mM Tris-MOPS, 1 mM EGTA, pH 7.4). Mitochondria were then purified by differential centrifugation (600*g* for 10 min) and supernatants were then centrifuged at 7000*g* for 10 min. For all tissues, the crude mitochondrial pellet was resuspended in an appropriate volume of MIB/MIB2 and mitochondrial protein concentration was determined using the bicinchoninic acid assay (Pierce BCA Protein Assay Kit −23225). Isolated mitochondria were protected from oxidation by a layer of argon gas and stored at −80 °C until analysis. Mitochondrial phospholipid and cardiolipin analysis were performed as described below for embryos.

Embryos were collected and immediately frozen in liquid nitrogen and protected from oxidation by a layer of argon gas and stored at −80 °C until analysis. Total phospholipid amount was determined with Corona CAD detection by calculating the concentration of each PL class (in µg/ml) compared to calibration ranges of commercial standards. Chromatographic system from ThermoFisher Scientific included a Dionex U-3000 RSLC system with 2 quaternary pumps, an autosampler and a column oven. The RSLC system was coupled on-line to a charged aerosol detector, Corona-CAD Ultra for the quantitative part of the study and a LTQ-Orbitrap Velos Pro for the lipidomic study (all from ThermoFisher). Liquid chromatography, mass spectrometry, phospholipid species identification and phospholipid species representation were performed as previously described [22]. For the identification of oxidized cardiolipin, we used a methodology set up for a previous study and described in [46]. More precisely, we found in *Hacd2*-KO embryos' samples the CL(72:8)(0) species (*m/z* 1463.962) previously observed in the study by Moulin et al. and its fragmentation spectra were identical. This revealed unambiguously the presence of oxidized cardiolipins in these samples. We further characterized the oxidized cardiolipins on the basis of the *m/z* of the ion obtained in fullscan (ionization in negative mode source resulting in an ion corresponding to cardiolipin having lost a hydrogen $[CL\text{-}H]^-$). Thanks to the very high resolution of the instrument (100 000 at m/z 400), it was possible to distinguish the ions corresponding to the different ionic species. By comparing experimental and simulated spectra, we discriminated in the isotope pools the ions from classical cardiolipins, from oxidized cardiolipins or from isotopes of either classical or oxidized cardiolipins. For the identification of the fatty acid composition of cardiolipins, the spectra were first obtained by electrospray ionization in negative mode. The ions obtained as a source were detected in the high-resolution orbital trap (fullscan, resolution of 100 000 at *m/z* 400) and corresponded to deprotonated cardiolipins, [CL-H]-. From these *m/z* ratios, we deduced the raw formula of CL, as well as the sum of the carbons and unsaturations of the fatty acyl chains. Then, cardiolipins were fragmented by Collision Induced Dissociation (CID) in the linear trap

(LTQ) of the instrument in a non-targeted, data-dependent mode. The MS2 and MS3 spectra obtained after ionization in negative mode allowed the identification of the fatty acid chains. During the analysis with the data-dependent mode, the most intense cardiolipins were fragmented, which corresponded to classical cardiolipins. A second analysis was performed, which consisted in a targeted fragmentation from a list of parent ions to specifically characterize the oxidized cardiolipins. The concentrations being very low, 2 samples were pooled from WT and *Hacd2*-KO embryos to obtain signals of sufficient intensity to perform a fragmentation. The MS2 spectra allowed the identification of the partial structures of the oxidized cardiolipins.
Results were analyzed with R software, version 3.6.3 and for the HeatMap with the Pretty Heatmaps R package version 1.0.12.

7.15. Determination of glucose and lactate blood concentration

Two small blood drops were obtained after a 0.5 mm section of tail tip. Blood glucose and lactate levels were measured using Contour XT glucometer (Bayer) and Lactate Scout (EKF Diagnostics for life) devices, respectively.

7.16. Temperature measurement

Infrared thermography was performed with the infrared digital thermographic camera E60: Compact Infrared Thermal Imaging Camera (FLIR) and data were analyzed by FLIR Quick Report software (FLIR ResearchIR Max 3.4; FLIR).
Internal temperature was obtained with a rectal probe adapted for pups (Bio-Thermo-Cis thermometer equipped with a Bio-Bret-3 rectal probe for mice; Bioseb).

8. QUANTIFICATION AND STATISTICAL ANALYSES

Data are plotted as individual values with mean ± s.e.m.. Datasets were analysed using GraphPad Prism. Outliers were identified using the ROUT method (Q = 5%). Differences between cleaned data were evaluated using a two-tailed unpaired non-parametric Mann—Whitney test with 95% confidence, corrected by the Bonferroni-Dunn method for multiple comparisons. Differences between groups were considered significant if the *P* value, or the corrected *P* value, was less than 0.05, with *: $P < 0.05$; **: $P < 0.01$; ***: $P < 0.001$ *versus* WT.

AUTHOR CONTRIBUTIONS

N. Khadhraoui: Conceptualization, Methodology, Formal analysis, Investigation, Resources, Writing - Original Draft, Visualization; **A. Prola**: Conceptualization, Methodology, Formal analysis, Investigation, Writing - Original Draft, Visualization; **A. Vandestienne**: Investigation, Writing - Review & Editing; **J. Blondelle**: Investigation, Resources, Writing - Review & Editing; **L. Guillaud**: Investigation, Writing - Review & Editing; **G. Courtin**: Investigation, Writing - Review & Editing; **M. Bodak**: Investigation, Writing - Review & Editing; **B. Prost**: Formal analysis, Investigation, Writing - Review & Editing; **H. Huet**: Investigation, Writing - Review & Editing; **M. Wintrebert**: Formal analysis, Writing - Review & Editing, Visualization; **C. Péchoux**: Investigation, Writing - Review & Editing, Visualization; **A. Solgadi**: Formal analysis, Resources, Writing - Review & Editing, Visualization, Supervision; **F. Relaix**: Writing - Review & Editing, Supervision, Project administration, Funding acquisition; **L. Tiret**: Conceptualization, Methodology, Formal analysis, Investigation, Resources, Writing - Original Draft, Visualization, Supervision, Project administration, Funding acquisition; **F. Pilot-Storck**: Conceptualization, Methodology, Formal analysis, Investigation, Resources, Writing - Original Draft, Visualization, Supervision, Project administration, Funding acquisition.

DATA AVAILABILITY

No data was used for the research described in the article.

ACKNOWLEDGEMENTS

The authors are grateful to Camille Laisne and Diana Gelperowic for taking care of mice; the Knock-Out Mouse Program (the "KOMP") for initially providing the ES cell lines carrying the floxed allele of *Hacd2*; Francina Langa-Vives (CIGM, Institut Pasteur) for the generation of *Hacd2*-knockout mice; Jean-Paul Pais de Barros and the LAP platform (Dijon, France) for lipidomic analyses; Martine Letheule for electron microscopy (Microscopy and Imaging Facility for Microbes, Animals and Foods MIMA2 platform, INRAE, Jouy-en-Josas, France); imaging platform from the Imagine Institute (Paris) for HREM analysis; Sigolène Meilhac and Lucile Miquerol for insightful discussions and mouse lines; Stéphane Zaffran and Marianne Gervais-Taurel for sharing reagents; Nicolas Blanchard-Gutton, Sophie Chateau, Caroline Choquet, Julie Da Silva, Christopher De Bono, Pierre Deshuilliers, Isabelle Lagrange, Rémi Mounier, Edouard Reyes-Gomez, Jean-Luc Servely and Sébastien Storck for technical help in FACS, histological and biochemical analyses; Geneviève Derumeaux for performing echocardiographic analysis; Roberto Motterlini and Roberta Foresti (U955-IMRB), and Santos Susin (Cordeliers Institute) for providing access to a Seahorse apparatus; Luisa Dandolo for providing access to the radioactivity platform of the Cochin Institute (Paris); Caroline Gilbert for sharing the infrared camera; Sigolène Meilhac and Véronique Duranthon for their advice during the thesis of N.K.
N.K.'s PhD fellowship has been financially supported by the French "Fondation pour la Recherche Médicale" (FRM). The work was primarily supported by the French "Agence Nationale de la Recherche" (ANR-12-JSV1-0005) and the "Association Française contre les Myopathies" (AFM 16143, Translamuscle I (# 19507) and Translamuscle II (# 22946)).

CONFLICT OF INTEREST

The authors declare that they have no conflict of interest.

APPENDIX A. SUPPLEMENTARY DATA

Supplementary data to this article can be found online at https://doi.org/10.1016/j.molmet.2023.101677.

REFERENCES

[1] Mitchell P. Coupling of phosphorylation to electron and hydrogen transfer by a chemi-osmotic type of mechanism. Nature 1961;191:144—8. https://doi.org/10.1038/191144a0.
[2] Frazier AE, Thorburn DR, Compton AG. Mitochondrial energy generation disorders: genes, mechanisms, and clues to pathology. J Biol Chem 2019;294(14):5386—95. https://doi.org/10.1074/jbc.R117.809194.
[3] McCormick EM, Zolkipli-Cunningham Z, Falk MJ. Mitochondrial disease genetics update: recent insights into the molecular diagnosis and expanding phenotype of primary mitochondrial disease. Curr Opin Pediatr 2018;30(6):714—24. https://doi.org/10.1097/MOP.0000000000000686.
[4] Vafai SB, Mootha VK. Mitochondrial disorders as windows into an ancient organelle. Nature 2012;491(7424):374—83. https://doi.org/10.1038/nature11707.
[5] Maldonado EM, Taha F, Rahman J, Rahman S. Systems biology approaches toward understanding primary mitochondrial diseases. Front Genet 2019;10:19. https://doi.org/10.3389/fgene.2019.00019.

[6] Murayama K, Shimura M, Liu Z, Okazaki Y, Ohtake A. Recent topics: the diagnosis, molecular genesis, and treatment of mitochondrial diseases. J Hum Genet 2019;64(2):113–25. https://doi.org/10.1038/s10038-018-0528-6.

[7] Cogliati S, Enriquez JA, Scorrano L. Mitochondrial cristae: where beauty meets functionality. Trends Biochem Sci 2016;41(3):261–73. https://doi.org/10.1016/j.tibs.2016.01.001.

[8] Lu Y-W, Claypool SM. Disorders of phospholipid metabolism: an emerging class of mitochondrial disease due to defects in nuclear genes. Front Genet 2015;6:3. https://doi.org/10.3389/fgene.2015.00003.

[9] Ikon N, Ryan RO. Cardiolipin and mitochondrial cristae organization. Biochim Biophys Acta Biomembr 2017;1859(6):1156–63. https://doi.org/10.1016/j.bbamem.2017.03.013.

[10] Paradies G, Paradies V, De Benedictis V, Ruggiero FM, Petrosillo G. Functional role of cardiolipin in mitochondrial bioenergetics. Biochim Biophys Acta Bioenerg 2014;1837(4):408–17. https://doi.org/10.1016/j.bbabio.2013.10.006.

[11] Hishikawa D, Hashidate T, Shimizu T, Shindou H. Diversity and function of membrane glycerophospholipids generated by the remodeling pathway in mammalian cells. J Lipid Res 2014;55(5):799–807. https://doi.org/10.1194/jlr.R046094.

[12] Renne MF, de Kroon AIPM. The role of phospholipid molecular species in determining the physical properties of yeast membranes. FEBS (Fed Eur Biochem Soc) Lett 2018;592(8):1330–45. https://doi.org/10.1002/1873-3468.12944.

[13] Sassa T, Kihara A. Metabolism of very long-chain Fatty acids: genes and pathophysiology. Biomol Ther 2014;22(2):83–92. https://doi.org/10.4062/biomolther.2014.017.

[14] Ohno Y, Suto S, Yamanaka M, Mizutani Y, Mitsutake S, Igarashi Y, et al. ELOVL1 production of C24 acyl-CoAs is linked to C24 sphingolipid synthesis. Proc Natl Acad Sci USA 2010;107(43):18439–44. https://doi.org/10.1073/pnas.1005572107.

[15] Denic V, Weissman JS. A molecular caliper mechanism for determining very long-chain fatty acid length. Cell 2007;130(4):663–77. https://doi.org/10.1016/j.cell.2007.06.031.

[16] Ikeda M, Kanao Y, Yamanaka M, Sakuraba H, Mizutani Y, Igarashi Y, et al. Characterization of four mammalian 3-hydroxyacyl-CoA dehydratases involved in very long-chain fatty acid synthesis. FEBS (Fed Eur Biochem Soc) Lett 2008;582(16):2435–40. https://doi.org/10.1016/j.febslet.2008.06.007.

[17] Abbasi-Moheb L, Westenberger A, Alotaibi M, Alghamdi MA, Hertecant JL, Ariamand A, et al. Biallelic loss-of-function HACD1 variants are a bona fide cause of congenital myopathy. Clin Genet 2021;99(4):513–8. https://doi.org/10.1111/cge.13905.

[18] Al Amrani F, Gorodetsky C, Hazrati L-N, Amburgey K, Gonorazky HD, Dowling JJ. Biallelic LINE insertion mutation in HACD1 causing congenital myopathy. Neurol Genet 2020;6(3):e423. https://doi.org/10.1212/NXG.0000000000000423.

[19] Blondelle J, Ohno Y, Gache V, Guyot S, Storck S, Blanchard-Gutton N, et al. HACD1, a regulator of membrane composition and fluidity, promotes myoblast fusion and skeletal muscle growth. J Mol Cell Biol 2015;7(5):429–40. https://doi.org/10.1093/jmcb/mjv049.

[20] Muhammad E, Reish O, Ohno Y, Scheetz T, Deluca A, Searby C, et al. Congenital myopathy is caused by mutation of HACD1. Hum Mol Genet 2013;22(25):5229–36. https://doi.org/10.1093/hmg/ddt380.

[21] Pelé M, Tiret L, Kessler J-L, Blot S, Panthier J-J. SINE exonic insertion in the PTPLA gene leads to multiple splicing defects and segregates with the autosomal recessive centronuclear myopathy in dogs. Hum Mol Genet 2005;14(11):1417–27. https://doi.org/10.1093/hmg/ddi151.

[22] Prola A, Blondelle J, Vandestienne A, Piquereau J, Denis RGP, Guyot S, et al. Cardiolipin content controls mitochondrial coupling and energetic efficiency in muscle. Sci Adv 2021;7(1):eabd6322. https://doi.org/10.1126/sciadv.abd6322.

[23] Toscano A, Emmanuele V, Savarese M, Musumeci O, Torella A, Conca E, et al. Pseudo-dominant inheritance of a novel homozygous HACD1 mutation associated with congenital myopathy: the first caucasian family. Neuromuscul Disord 2017;27:S173. https://doi.org/10.1016/j.nmd.2017.06.290.

[24] Wang B, Pelletier J, Massaad MJ, Herscovics A, Shore GC. The yeast split-ubiquitin membrane protein two-hybrid screen identifies BAP31 as a regulator of the turnover of endoplasmic reticulum-associated protein tyrosine phosphatase-like B. Mol Cell Biol 2004;24(7):2767–78. https://doi.org/10.1128/mcb.24.7.2767-2778.2004.

[25] Wei L, Weng S, Lu X, Zhu S, Yang Q, Chen YQ. 3-Hydroxyacyl-CoA dehydratase 2 deficiency confers resistance to diet-induced obesity and glucose intolerance. Biochem Biophys Res Commun 2022;605:134–40. https://doi.org/10.1016/j.bbrc.2022.03.057.

[26] Palis J, Robertson S, Kennedy M, Wall C, Keller G. Development of erythroid and myeloid progenitors in the yolk sac and embryo proper of the mouse. Development (Cambridge, England) 1999;126(22):5073–84.

[27] Krug EL, Runyan RB, Markwald RR. Protein extracts from early embryonic hearts initiate cardiac endothelial cytodifferentiation. Dev Biol 1985;112(2):414–26. https://doi.org/10.1016/0012-1606(85)90414-2.

[28] Kelly RG. Cardiac development and animal models of congenital heart defects. In: Rickert-Sperling S, Kelly RG, Driscoll DJ, editors. Congenital heart diseases : the broken heart : clinical features, human genetics and molecular pathways. Springer-Verlag; 2016. p. 3–9.

[29] Kisanuki YY, Hammer RE, Miyazaki J, Williams SC, Richardson JA, Yanagisawa M. Tie2-Cre transgenic mice: a new model for endothelial cell-lineage analysis in vivo. Dev Biol 2001;230(2):230–42. https://doi.org/10.1006/dbio.2000.0106.

[30] Saga Y, Miyagawa-Tomita S, Takagi A, Kitajima S, Miyazaki Ji, Inoue T. MesP1 is expressed in the heart precursor cells and required for the formation of a single heart tube. Development 1999;126(15):3437–47.

[31] Muzumdar MD, Tasic B, Miyamichi K, Li L, Luo L. A global double-fluorescent Cre reporter mouse. Genesis (New York, N.Y.: 2000) 2007;45(9):593–605. https://doi.org/10.1002/dvg.20335.

[32] Delavallée L, Mathiah N, Cabon L, Mazeraud A, Brunelle-Navas M-N, Lerner LK, et al. Mitochondrial AIF loss causes metabolic reprogramming, caspase-independent cell death blockade, embryonic lethality, and perinatal hydrocephalus. Mol Metabol 2020;40:101027. https://doi.org/10.1016/j.molmet.2020.101027.

[33] Vrbacký M, Kovalčíková J, Chawengsaksophak K, Beck IM, Mráček T, Nůsková H, et al. Knockout of Tmem70 alters biogenesis of ATP synthase and leads to embryonal lethality in mice. Hum Mol Genet 2016;25(21):4674–85. https://doi.org/10.1093/hmg/ddw295.

[34] Vincent AE, Ng YS, White K, Davey T, Mannella C, Falkous G, et al. The spectrum of mitochondrial ultrastructural defects in mitochondrial myopathy. Sci Rep 2016;6(1):30610. https://doi.org/10.1038/srep30610.

[35] Gómez Rodríguez A, Talamonti E, Naudi A, Kalinovich AV, Pauter AM, Barja G, et al. Elovl2-Ablation leads to mitochondrial membrane fatty acid remodeling and reduced efficiency in mouse liver mitochondria. Nutrients 2022;14(3):559. https://doi.org/10.3390/nu14030559.

[36] Zhang M, Mileykovskaya E, Dowhan W. Cardiolipin is essential for organization of complexes III and IV into a supercomplex in intact yeast mitochondria. J Biol Chem 2005;280(33):29403–8. https://doi.org/10.1074/jbc.M504955200.

[37] Zhang M, Mileykovskaya E, Dowhan W. Gluing the respiratory chain together. Cardiolipin is required for supercomplex formation in the inner mitochondrial membrane. J Biol Chem 2002;277(46):43553–6. https://doi.org/10.1074/jbc.C200551200.

[38] Zhang J, Guan Z, Murphy AN, Wiley SE, Perkins GA, Worby CA, et al. Mitochondrial phosphatase PTPMT1 is essential for cardiolipin biosynthesis. Cell Metabol 2011;13(6):690–700. https://doi.org/10.1016/j.cmet.2011.04.007.

[39] Kasahara T, Kubota-Sakashita M, Nagatsuka Y, Hirabayashi Y, Hanasaka T, Tohyama K, et al. Cardiolipin is essential for early embryonic viability and mitochondrial integrity of neurons in mammals. FASEB (Fed Am Soc Exp Biol) J: Off Publ Fed Am Soc Exp Biol 2020;34(1):1465–80. https://doi.org/10.1096/fj.201901598R.

[40] Maguire JJ, Tyurina YY, Mohammadyani D, Kapralov AA, Anthonymuthu TS, Qu F, et al. Known unknowns of cardiolipin signaling: the best is yet to come. Biochim Biophys Acta Mol Cell Biol Lipids 2017;1862(1):8—24. https://doi.org/10.1016/j.bbalip.2016.08.001.

[41] Falabella M, Vernon HJ, Hanna MG, Claypool SM, Pitceathly RDS. Cardiolipin, mitochondria, and neurological disease. Trends Endocrinol Metabol 2021;32(4):224—37. https://doi.org/10.1016/j.tem.2021.01.006.

[42] Vähäheikkilä M, Peltomaa T, Róg T, Vazdar M, Pöyry S, Vattulainen I. How cardiolipin peroxidation alters the properties of the inner mitochondrial membrane? Chem Phys Lipids 2018;214:15—23. https://doi.org/10.1016/j.chemphyslip.2018.04.005.

[43] Rantakari P, Lagerbohm H, Kaimainen M, Suomela J-P, Strauss L, Sainio K, et al. Hydroxysteroid (17{beta}) dehydrogenase 12 is essential for mouse organogenesis and embryonic survival. Endocrinology 2010;151(4):1893—901. https://doi.org/10.1210/en.2009-0929.

[44] Mohun TJ, Weninger WJ. Embedding embryos for high-resolution episcopic microscopy (HREM). Cold Spring Harb Protoc 2012;2012(6):prot069583. https://doi.org/10.1101/pdb.prot069583.

[45] Malgoyre A, Prola A, Meunier A, Chapot R, Serrurier B, Koulmann N, et al. Endurance is improved in female rats after living high-training high despite alterations in skeletal muscle. Front Sport Active Liv 2021;3.

[46] Moulin M, Solgadi A, Veksler V, Garnier A, Ventura-Clapier R, Chaminade P. Sex-specific cardiac cardiolipin remodelling after doxorubicin treatment. Biol Sex Differ 2015;6(1):1—14. https://doi.org/10.1186/s13293-015-0039-5.

